Journal of Sound and Vibration 339 (2015) 123–142

Contents lists available at ScienceDirect

Journal of Sound and Vibration

journal homepage: www.elsevier.com/locate/jsvi

Optimal rigid and porous material distributions for noise barrier by acoustic topology optimization

Ki Hyun Kim, Gil Ho Yoon *

School of Mechanical Engineering, Hanyang University, Seoul, Republic of Korea

ARTICLE INFO

Article history:
Received 18 June 2014
Received in revised form
8 November 2014
Accepted 24 November 2014
Handling Editor: L.G. Tham
Available online 16 December 2014

ABSTRACT

This research applies acoustic topology optimization (ATO) for noise barrier design with rigid and porous materials. Many researchers have investigated the pressure attenuation phenomena of noise barriers under various geometric, material, and boundary conditions. To improve the pressure attenuation performance of noise barriers, size and shape optimization have been applied, and ATO methods have been proposed that allow concurrent size, shape, and topological changes of rigid walls and cavities. Nevertheless, it is unusual to optimize the topologies of noise barriers by considering the pressure attenuation effect of a porous material. The present research develops a new ATO considering both porous and rigid materials and applies it to the discovery of optimal topologies of noise barriers composed of both materials. In the present approach, the noise absorption characteristics of porous materials are numerically modeled using the Delany–Bazley empirical material model, and we also investigate the effects of some interpolation functions on optimal material distributions. Applying the present ATO approach, we found some novel noise barriers optimized for various geometric and environmental conditions.

1. Introduction

This research studies the optimal material distributions of rigid and porous materials for noise barriers. Optimization topics in noise barrier design were widely discussed and recently, acoustic topology optimization techniques were used to obtain the topological design result of noise barrier. But previous acoustic topology optimization researches for noise barrier only considered the design of rigid material for the shapes of noise barrier. In other words noise barrier design considering both rigid and porous materials as design requirements in the acoustic topology optimization was not researched yet. In the present research, we applied a gradient-based optimizer to determine the optimal topologies and distributions of rigid and porous materials within a noise barrier. Also some optimization examples considering different acoustical conditions and design requirements are investigated.

Within the context of current industrial development, the evolution of urban areas and the development of transportation substructures has led to noise becoming one of the most serious problems in our society. Environmental noise in particular is considered a serious issue from social, environmental, and public health perspectives. Environmental noise usually involves sound propagation in a complex and unsteady fluidic medium where many physical effects come into play in sound propagation. This makes the control of environmental noise a tremendously challenging task. So far, engineers

* Corresponding author.
E-mail addresses: ghy@hanyang.ac.kr, gilho.yoon@gmail.com (G.H. Yoon).

http://dx.doi.org/10.1016/j.jsv.2014.11.030
0022-460X/

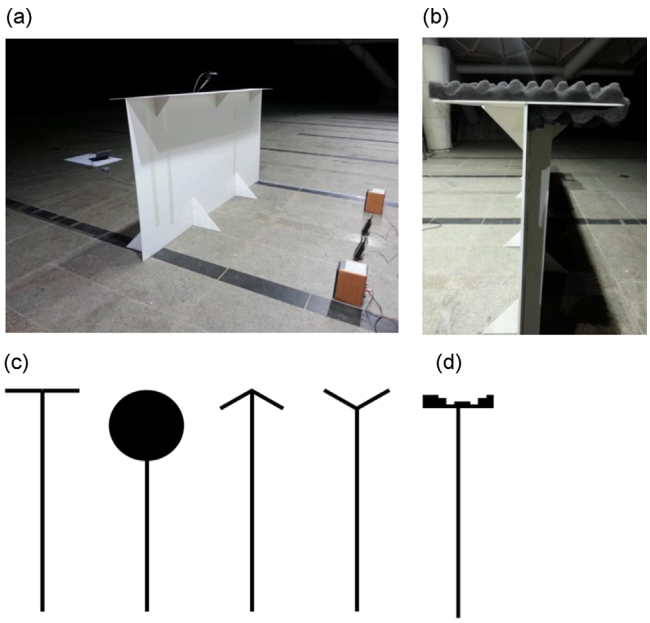

Fig. 1. Noise barrier. (a) Noise barrier experiment with T-shaped barrier, (b) T-shaped barrier with porous material, (c) other barrier types (from left to right, T-shaped, cylinder-shaped, arrow-shaped, and y-shaped), and (d) T-shaped barrier with quadratic residue diffuser (QRD).

have three main options to control noise: reduce the radiated sound power, protect the receiver from the incoming noise, and prevent noise propagation by modifying the propagation path. One easy and popular way to implement the third strategy, i.e., preventing noise propagation, is to use a noise barrier (sometimes called a screen or noise protection) between the noise source and the receiver. Compared with the other measures, noise barriers are a lightweight, easy-to-install, and cost-effective way to moderate noise pollution. Noise barriers are therefore commonly used for the most public applications to provide noise absorption and sound reflection. To calculate the efficiency of a noise barrier accurately, with the hope of building a better barrier, much fundamental and experimental research has been conducted [1–3]. Most of this research has concluded that the common T-shaped barrier shown in Fig. 1 has the most effective geometry [4,5], and some research has been conducted to heuristically change the details of its geometric parameters to optimize acoustic attenuation in a number of noise environments [6,7]. In addition, some extended research has been done to change the profiles of the upper surface of a T-shape barrier with both rigid and porous structures [8–10].

Much experimental and computational research has been conducted to find an optimal noise barrier. In [4], the performances of barriers with different profiles and surface conditions were calculated using the boundary element method. In our reading, one key finding is that the use of soft edges formed with a porous material can significantly influence the efficiency of noise barriers without significantly altering their shape. Furthermore, a T-shaped barrier with soft edges might provide the highest barrier performance for medium- and high-frequency ranges. In [5], a series of experiments was performed to compare the performances of rectangular, T-shaped, and cylindrical-edged noise barriers with rigid walls covered by soft porous surfaces. In that research, the most efficient design was a T-shaped structure with a soft upper surface (Fig. 1(a and b)). A uniform series of wells in the upper surface of a T-shaped barrier was found to provide barrier performance equal to that of a soft upper surface over a wide range of frequencies. In [11], the performances of a T-shaped structure, a cylinder-shaped structure, an arrow-shaped structure, and a y-shaped structure (Fig. 1(b)) were investigated with quadratic residue diffuser (QRD) tops (Fig. 1(c)). The use of a QRD structure on the top surface of a barrier improved sound absorption significantly compared with a simple porous cover. The profile showing the best performance with the QRD structure is also based on a T-shaped barrier. In [12], a random sequence diffuser (RSD) was designed to determine a better depth sequence, and the results showed that the installment of an RSD structure improved barrier performance compared with a Schroeder diffuser (the most popular QRD) and a primitive root diffuser. Diffuser performance can also be improved by covering the top surface or inside of the wells with perforated sheets. In [13], the effects of the positions of the sound source and the receiver on noise attenuation performance are investigated for a T-shaped noise barrier. Furthermore, the effects of the height and width of a T-shaped barrier and absorptive material are considered. Thus existing research suggests that the most efficient noise barrier is probably T-shaped with some absorbing structures.

From a design point of view, some relevant research applies mathematical or evolutionary optimization algorithms with computational analysis methods to improve the performances of various barriers [14–16]. In [17], an evolutionary optimization method was used to improve the acoustical efficiency of a T-shaped barrier whose top was covered with a series of wells. In this research, the geometric parameters, such as the depths of the wells, were optimized for barriers with only rigid material and for barriers with porous material. In [18], researchers optimized the cross-section of a noise barrier

by considering its acoustical performance and also the economic feasibility of using various materials for different barrier shapes based on a genetic algorithm. From an optimization point of view, these studies can be regarded as size and shape optimization schemes, respectively.

One limitation of existing optimization schemes is that an initial design or sound barrier should be provided by scientists or engineers. Without preliminary designs, optimization methods cannot be applied efficiently. To surmount this limitation of requiring initial designs, topology optimization (TO) methods have been developed [19,20]. TO methods were originally developed for structural optimization [19,20], but they have been applied to many wave-related optimization problems [21–26] as well. In [27], a TO method is presented for the design of an acoustic horn. In [28], microstructure is optimized by topology optimization method with respect to sound power radiation from a vibration macrostructure at a single and a band of excitation frequencies. In [29], the levelset-based topology optimization method is proposed for acoustic–structure interaction. In [30], acoustic meta-materials with negative bulk modulus are designed using a TO method. In [31], TO is used to minimize the fluid–structure interactions of a plate coupled with an acoustic cavity. In [32], TO is applied to the design problems of an expansion chamber and an outdoor acoustic barrier considering both single barriers and double barriers. In [33], an acoustic topology optimization (ATO) method considering humans' subjective conception of sound is presented. With the ATO method, various layouts of noise barriers are presented with different source and receiver positions but without considering the effect of porous materials.

Despite some relevant research about noise barrier analysis and size optimization with the application of porous (absorptive) material, previous ATO research considered the distribution of only rigid materials. In other words, TO results for noise barriers considering the distribution of both rigid and porous materials have not yet been determined. This research suggests an ATO method for a noise barrier with both rigid and porous materials with various geometric and boundary conditions [34]. In the present study, it was important to discover a proper interpolation function to distribute rigid and porous material simultaneously. Thus we researched several interpolation functions and studied their characteristics in designing the noise barrier.

The layout of the paper is organized as follows: in Section 2, an acoustic finite element method using the Helmholtz equation is reviewed, and the empirical Delany–Bazley material model is applied to consider the effects of porous material properties in the framework of the Helmholtz equation. The analysis example provides the acoustic characteristics of a standard straight rigid noise barrier of interest. In Section 3, the TO formulation and material interpolation functions for the two types of acoustic materials are provided. A complex sensitivity analysis is derived for the design variables representing the material layout to allow use of a gradient-based optimization algorithm. TO results for various acoustical conditions are provided in Section 4. Finally, we summarize the optimization results and discuss our findings in the conclusion.

2. Acoustic finite element procedures for the simulation of a noise barrier

2.1. Helmholtz equation for sound radiation problem

To solve the 2D acoustic radiation problem, the following Helmholtz equation assuming harmonically varying pressure is considered.

$$\nabla \cdot \left(\frac{1}{\rho}\nabla p\right) + \frac{\omega^2}{\rho c^2} p = 0 \ \text{ on } \ \Omega \tag{1}$$

where p, ρ, c, and ω are the spatially-varying pressure in the acoustic domain Ω, the local density, the local speed of sound, and the angular velocity of the sound wave, respectively. To solve the Helmholtz equation with the finite element method, the weak formulation of (2) is used.

$$\int_{\Omega} \frac{1}{\rho}\nabla \tilde{p} \cdot \nabla p \, d\Omega - \int_{\Omega} \frac{\omega^2}{\rho c^2} \tilde{p} p \, d\Omega = \int_{\Gamma} \frac{1}{\rho} \tilde{p} \nabla p \cdot \mathbf{n} \, d\Gamma \tag{2}$$

In this equation, $\mathbf{n}$ is the outward unit normal vector at the boundary of the acoustic domain Γ. The virtual pressure is denoted by $\tilde{p}$. Commonly, Neumann and Dirichlet boundary conditions are imposed on the weak formulation. For the special boundary condition without sound reflection, i.e., Sommerfeld boundary condition, $\nabla p \cdot \mathbf{n}$ can be transformed into $-\mathrm{i}\rho\omega V_b$, where V_b is the particle velocity in the outward normal direction at the boundary. For instance, we can ponder a semicircle-shaped acoustic domain, as shown in Fig. 2. Because the acoustic domain is formed of square elements, the acoustic boundary is not curved. Therefore for the implementation of the Sommerfeld boundary condition at the rim of the semicircle in Fig. 2, the particle velocity normal to the boundary, V_b, needs to be expressed in terms of its orthogonal projection component, V_r (the particle velocity of the cylindrical wave), in the radial direction from the center of the semicircle as shown in Fig. 2. This projection is essential because V_b need to be expressed in terms of p with the approximate pressure–velocity relation for the cylindrical wave relation to solve the matrix equation for p. Mathematically, the following conditions from (3) to (4) are imposed here. The angle between V_b and V_r is denoted by θ.

$$\text{Sommerfeld boundary condition: } \nabla p \cdot \mathbf{n} = -\mathrm{i}\rho\omega V_b = -\mathrm{i}\rho\omega \cos\theta \times V_r \tag{3}$$

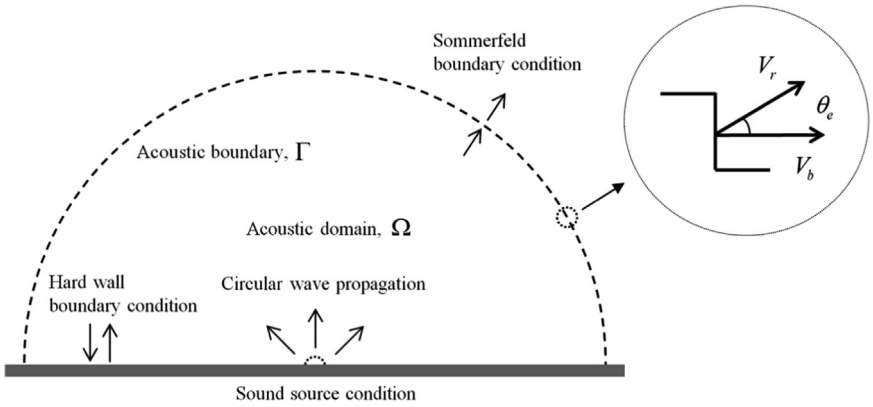

Fig. 2. Acoustic domain and acoustic boundary conditions for cylindrical wave propagation.

$$\text{Approximated pressure}-\text{velocity relation for cylindrical wave: } V_r = \frac{1}{\rho c} p \tag{4}$$

Equation in (4) can be obtained by considering the cylindrical wave propagation as follows [35]:

$$\left(\frac{\partial^2}{\partial r^2}+\frac{1}{r}\frac{\partial}{\partial r}+\frac{1}{r^2}\frac{\partial^2}{\partial \theta^2}+\frac{\partial^2}{\partial z^2}\right)p = \frac{1}{c^2}\frac{\partial^2 p}{\partial t^2} \tag{5}$$

For the cylindrically symmetrically propagating outgoing wave, the pressure field can be expressed as a function of radial distance.

$$p(r) = AH_0^{(2)}(kr) \tag{6}$$

where $H_0^{(2)}$ is the Hankel function (commonly, the superscript (1) indicates incoming wave whereas (2) indicates outgoing wave) and the asymptotic approximation to the Hankel function, with k_r»1, becomes as follows:

$$p(r) = A\sqrt{\frac{2}{\pi kr}}e^{j(-kr+\pi/4)} \tag{7}$$

With the condition of $k_r \gg 1$, the asymptotic approximations of the above Hankel functions show that

$$z \to \rho c \tag{8}$$

where z is the acoustic impedance. Then the following is assumed.

$$V_r = \frac{1}{\rho c} p \tag{9}$$

As the radii of the curvature of the constant phase contours are much larger than a wavelength, the waveform can be assumed as a plane wave.

2.2. Finite element method for Helmholtz equation

For the finite element simulation, the linear pressure p and its spatial differential ∇p at a spatial point in the acoustic domain are approximated by the nodal pressure values of the square element, i.e., Q4 element, as (10). The column vector of the nodal pressures in the eth element, the shape function matrix, and the differentiated shape function matrix are denoted by $\mathbf{p}_e$, $\mathbf{N}$, and $\mathbf{B}$, respectively. Then the matrix equation in (11) is obtained.

$$p \approx \mathbf{N}\mathbf{p}_e, \quad \nabla p \approx \mathbf{B}\mathbf{p}_e \tag{10}$$

$$\int_{\Omega_e}\frac{1}{\rho}\mathbf{B}^T\mathbf{B}\mathbf{p}_e \, d\Omega - \int_{\Omega_e}\frac{\omega^2}{\rho c^2}\mathbf{N}^T\mathbf{N}\mathbf{p}_e \, d\Omega = -i\omega\int_{\Gamma_e}\frac{1}{\rho c}\cos\theta \mathbf{N}^T\mathbf{N}\mathbf{p}_e \, d\Gamma \tag{11}$$

$$[\mathbf{K}-\omega^2\mathbf{M}+i\omega\mathbf{F}^{radiation}]\mathbf{p} = 0 \tag{12}$$

$$\mathbf{k}_e = \frac{1}{\rho_e}\int_{\Omega_e}\mathbf{B}^T\mathbf{B} \, d\Omega, \quad \mathbf{m}_e = \frac{1}{\rho_e c_e^2}\int_{\Omega_e}\mathbf{N}^T\mathbf{N} \, d\Omega, \quad \mathbf{f}_e^{radiation} = \frac{1}{\rho_e c_e}\int_{\Gamma_e}\cos\theta_e \mathbf{N}^T\mathbf{N} \, d\Gamma \tag{13}$$

As the material properties for each element are assumed to be constants, the three integral terms in (11) can be calculated. In (13), $\mathbf{k}_e$, $\mathbf{m}_e$, and $\mathbf{f}_e^{radiation}$ are defined as local stiffness, mass, and force matrices for the eth element, respectively. The density, the wave speed, the domain, and the boundary of the eth element are defined as ρ_e, c_e, Ω_e, and Γ_e, respectively.

The angle between V_b and V_r at the eth element is θ_e. These local matrices are assembled into the global matrices for the entire domain. Note that the force matrix, $\mathbf{f}_e^{radiation}$, is superposed only for the elements in the acoustic boundary. The final governing equation is summarized as (12). The superposed global matrices for the local matrices $\mathbf{k}_e$, $\mathbf{m}_e$, and $\mathbf{f}_e^{radiation}$ are denoted by $\mathbf{K}$, $\mathbf{M}$, and $\mathbf{F}^{radiation}$, respectively.

2.3. Acoustic material properties for air, rigid material, and fibrous material

To simulate the pressure attenuation with different acoustic materials in (13), density, bulk modulus, and characteristic impedance should be assigned to each finite element. For the finite elements for air, the density (ρ_a) is set to 1.25 kg/m^3 and the wave speed (c_a) is set to 343 m/s. The other properties, such as bulk modulus $B_a(=\rho_a c_a^2)$ and characteristic impedance $Z_a(=\rho_a c_a)$, are calculated accordingly.

For a simulation of a rigid domain, we neglect the mutual coupling between elastic structure and fluidic domain, and we numerically set the impedance of the boundaries very high to model the sound reflection of a rigid wall. To implement this feature, the density ρ_r and bulk modulus B_r are set to very large numbers but not large enough to cause numerical instability. Then the boundaries of the rigid domain completely reflect the incoming wave and can be assumed as hard walls. Based on the research in [36], the material properties of a rigid domain are set as follows:

$$\rho_r = \rho_a \cdot 10^7, \quad B_r = B_a \cdot 10^9 \tag{14}$$

Many numerical approaches have been proposed to model the pressure attenuation of porous materials. Among some theories, we have used the Delany–Bazley empirical material model, which considers pressure absorbing materials such as fiber, glass, and wood–wool with flow resistivity [37,38]. In this empirical material model, the bulk modulus and impedance are formulated by the following equations.

$$k_p = k_a\left(1+0.0978\left(\frac{\rho_a f}{\sigma}\right)^{-0.7} - \mathrm{i}0.189\left(\frac{\rho_a f}{\sigma}\right)^{-0.595}\right) \tag{15}$$

$$Z_p = Z_a\left(1+0.0571\left(\frac{\rho_a f}{\sigma}\right)^{-0.734} - \mathrm{i}0.087\left(\frac{\rho_a f}{\sigma}\right)^{-0.732}\right) \tag{16}$$

$$f = \frac{\omega}{2\pi}, \quad 0.01 < \frac{\rho_a f}{\sigma} < 1.0 \tag{17}$$

$$\rho_p = \frac{k_p Z_p}{\omega}, \quad c_p = \frac{\omega}{k_p}, \quad B_p = \rho_p c_p^2 \tag{18}$$

In (15) and (16), the wave number of the porous material k_p and the characteristic impedance of porous material Z_p can be calculated with the airflow resistivity σ and the frequency f. In the noise barrier design examples given in Section 4, airflow resistivity σ is set to 1400 Rayleighs/m to consider the material property of wood–wool [39].

2.4. Analysis example: pressure propagation of a semi-circle

In order to verify the accuracy of the finite element method and the boundary conditions, it is possible to compare the pressure distributions of the finite element solution and the approximated Hankel function which is the analytical solution for the cylindrical wave propagation. The Hankel function can be summarized as follows:

$$p(r) = A\sqrt{\frac{2}{\pi kr}}e^{\mathrm{i}(-kr+\pi/4)} \tag{19}$$

where A is a constant determined by the boundary condition. In the above solution, the real part and the imaginary part becomes infinite when the distance, r, becomes zero. Therefore, we chose A such that the above Hankel solution at an arbitrary chosen r becomes that of the finite element solution and compare the accuracy of the finite element solution at the other distances. In our paper, A becomes 0.4 when the Hankel solution becomes the pressure of the finite element solution with the pressure input $1+\mathrm{i}$ (Pa) at 6 m distance. The following figures compare the accuracy of the finite element solution. As illustrated, the finite element solution is accurate enough (Fig. 3).

To see the influence of a straight barrier and set its performance as a reference, an acoustic simulation is performed for a semi-sphere domain with a straight rigid barrier, as shown in Fig. 4. A noise source is located at the center of the semicircle whose bottom is ideally grounded and whose upper boundary is modeled with no reflection. The analysis domain is discretized by 0.025 m $\times$ 0.025 m 4-node quad elements. For the simulation of the sound barrier at a road, the distance between the sound source and the barrier X_{SR} is set to 4 m, and the barrier height H_B is varied from 1 m to 3 m. The sound pressures of the source and the receiver are denoted by p_{sourse} and $p_{receiver}$, respectively.

Without loss of generality, we selected 100 Hz as the target frequency for structural topology optimization of the noise barrier. As the frequency ranges of many road traffic noises have low frequency ranges, 100 Hz is chosen as the target

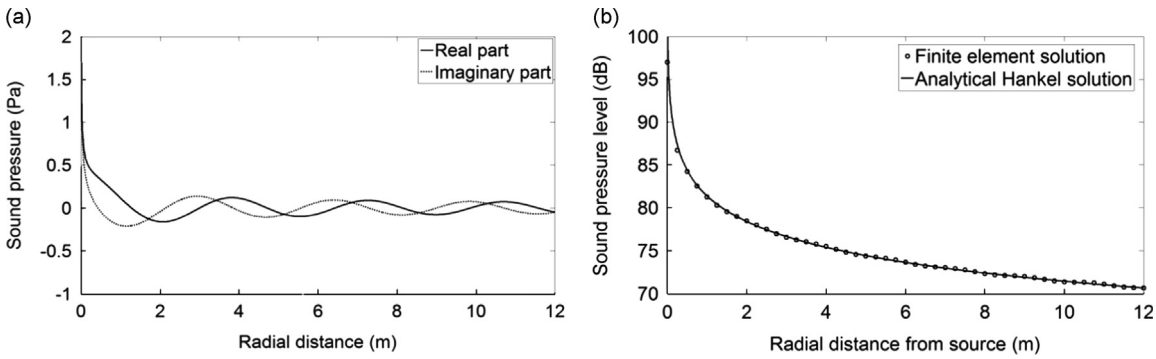

Fig. 3. Solution verification. (a) The real and imaginary parts of the sound pressure of the analytical Hankel solution, and (b) comparison of the finite element solution and the Hankel solution. (the pressure input 1+i (Pa), $A=0.4$).

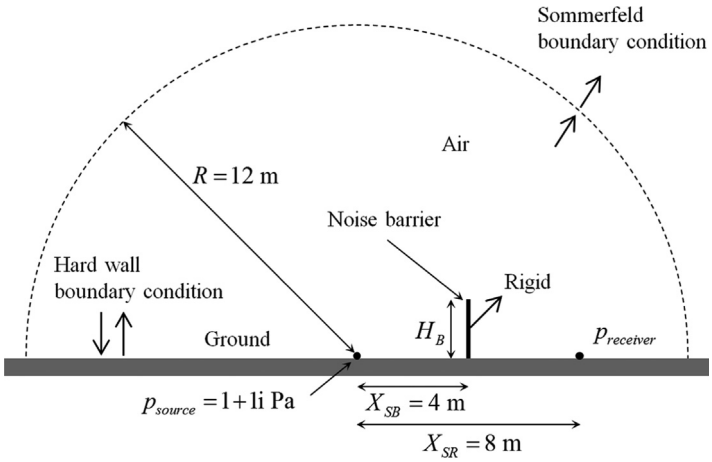

Fig. 4. Acoustic domain for noise barrier analysis. (R: radius of the analysis domain (12 m), X_{SB}: the distance between the sound source and the barrier (4 m), H_B: the barrier height (1 m, 2 m, and 3 m), p_{sourse}: sound pressure of noise, $p_{receiver}$: sound pressure at receiver, finite element mesh size (0.025 m by 0.025 m)).

frequency of the optimization of noise barrier. From the traffic noise spectrum analyses [40–42], it is known that the low frequency region between 63 Hz and 125 Hz in 1/3 octave band indicates higher noise level than the high frequency region.

A sound barrier 1 m tall was modeled, and an acoustic finite element simulation was performed with a 100 Hz sound source. The sound pressure and sound pressure level (SPL) distributions are shown in Fig. 5(a) and (b). Fig. 5(c) shows the SPL with the distance from the barrier. As expected, the magnitude of the sound pressure is reduced with help from the noise barrier. It should be mentioned that the ground is modeled as the ideal ground. In real application, the acoustic behavior of a surface can affect the performance of the barrier, which implies that one can control the noise magnitude at a receiver position by changing the acoustic behavior of surface.

To our knowledge, the typical sound barriers such as T-shape, arrow-shape and Y-shape have been used widely. To test the performances of these barriers, the performances of the optimized design and the designs except the circle shape barrier are tested; one of the reasons to exclude the circle shape barrier is that the mass ratio of the circle shape barrier is not met with that of the optimized one. For a fair comparison with the Y-shape sound barrier, the designs of T-shape 2 and T-shape 3 modified from the typical T-shape 1 design are considered and the sound pressure levels at the receiver point are compared. As the typical sound barriers are made of rigid elements, only the performance of the optimized design with rigid elements is compared with those of the typical sound barriers. The geometry of the Y-shape sound barrier is devised in order to cover the top side and the left and right sides of the design domain. The T-shape 1 barrier is constructed with 41 solid elements or about 2.5percent which is smaller than the mass of the present design. The arrow shape sound barrier and the Y-shape sound barrier use more mass than that of the present one to cover the design domain. As shown in the figure and the table, the present design performs better than the other designs (Figs. 6 and 7).

Here we should mention that the sound blocking performances are influenced by the finite element modeling of the oblique structure. For example, the performances of the arrow shape and the Y-shape barriers are compared with the structures having point contacts (or hinged type barrier) and the structures having area contacts. As shown, the variations in the performances are observed depending on the finite element modeling.

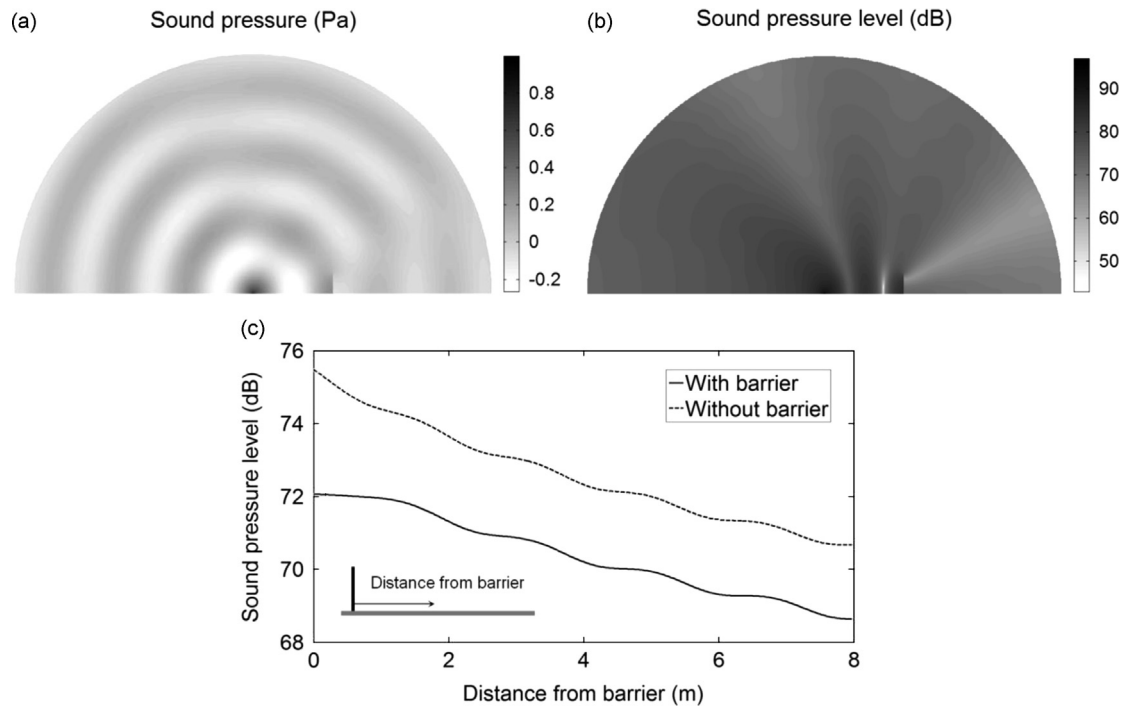

Fig. 5. Acoustic finite element analysis with 1 m sound barrier at 100 Hz frequency: (a) the sound pressure distribution, (b) sound pressure level (SPL) distribution, and (c) SPL on the ground with the distance from the barrier.

3. Acoustic topology optimization for the sound barrier

This section develops an optimization formulation and the material interpolation function of the ATO method to design an optimal sound barrier layout composed of both rigid and porous materials. For a gradient-based optimizer, the method of moving asymptotes (MMA) is used [43].

3.1. Optimization problem formulation

The purpose of the optimization problem is to find the best material layout inside a design domain to minimize the SPL at a receiver subject to given material ratios as follows:

$$\begin{aligned} &\text{Min } SPL_r(\boldsymbol{\gamma}) \\ &\text{Subject to } \sum_{e=1}^{NE} \gamma_{e,1} v_e \Big/ \sum_{e=1}^{NE} v_e - \beta_{rigid} \le 0 \\ &\sum_{e=1}^{NE} \gamma_{e,2} v_e \Big/ \sum_{e=1}^{NE} v_e - \beta_{porous} \le 0 \end{aligned} \tag{20}$$

$$\boldsymbol{\gamma} = [\underbrace{\gamma_{1,1}, \ldots, \gamma_{NE,1}}_{\text{For rigid material}}, \underbrace{\gamma_{1,2}, \ldots, \gamma_{NE,2}}_{\text{For porous material}}], \quad 0 \le \gamma_{e,1}, \gamma_{e,2} \le 1 \tag{21}$$

where SPL_r is the SPL at the receiver point. The design variables are $\boldsymbol{\gamma}$ assigned to the NE finite elements. Because one of the three states, i.e., air, rigid material, or porous material, should be determined, the two design variables $\gamma_{e,1}$ and $\gamma_{e,2}$ for the eth element having v_e volume are assigned in the framework of the solid isotropic material with penalization (SIMP) approach. The allowable mass ratios of the rigid and porous structures to the design domain are β_{rigid} and β_{porous}, respectively.

3.2. Material interpolation function

Because the original TO problem with discrete design variables is difficult to solve mathematically and numerically, it is common to relax it using continuous design variables with the continuous interpolation function. Therefore the criteria in choosing the form of the interpolation function for the present subject are that it should be easy to implement, and it should discover a distinctly converged layout among air, rigid material, and porous material with few intermediate states. To do

(a)

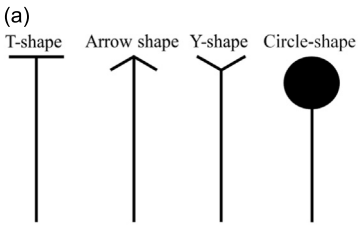

(b)

TO design	T-shape 1	T-shape 2	T-shape 3	Arrow shape	Y-shape
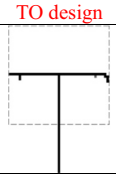	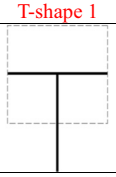			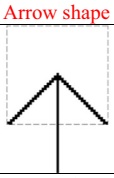	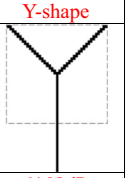
SPL_r : 64.03 dB (100 Hz)	100 Hz: 64.24 dB	66.50 dB	64.50 dB	65.01 dB	64.85 dB
	200 Hz: 57.30 dB	59.45 dB	58.86 dB	67.83 dB	56.99 dB
	300 Hz: 62.08 dB	53.81 dB	59.46 dB	66.36 dB	55.34 dB
Number of rigid elements element: 49	41	40	60	79	79

Fig. 6. (a) Typical sound barriers and (b) the implementations of the sound barriers.

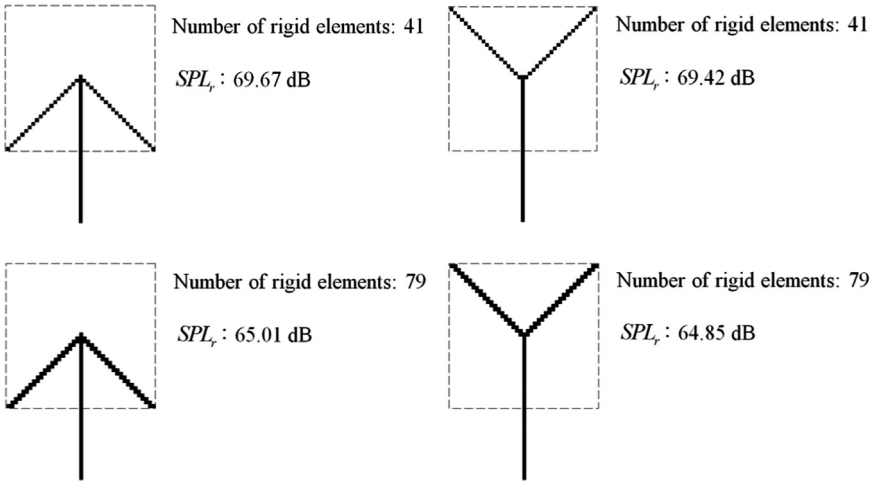

Fig. 7. The effects of the oblique modeling in the finite element analysis.

this, we consider that the density and bulk modulus are interpolated with the following reciprocal functions as follows [36,44]:

$$\text{Density: } \frac{1}{\rho_e(\gamma_{e,1},\gamma_{e,2})} = \frac{1}{\rho_a} + \left(\frac{1}{\rho_r} - \frac{1}{\rho_a}\right) \times \phi_{e,1}(\gamma_{e,1},\gamma_{e,2}) + \left(\frac{1}{\rho_p} - \frac{1}{\rho_a}\right) \times \phi_{e,2}(\gamma_{e,1},\gamma_{e,2}) \tag{22}$$

$$\text{Bulk modulus: } \frac{1}{B_e(\gamma_{e,1},\gamma_{e,2})} = \frac{1}{B_a} + \left(\frac{1}{B_r} - \frac{1}{B_a}\right) \times \phi_{e,1}(\gamma_{e,1},\gamma_{e,2}) + \left(\frac{1}{B_p} - \frac{1}{B_a}\right) \times \phi_{e,2}(\gamma_{e,1},\gamma_{e,2}) \tag{23}$$

where the density and bulk modulus for the eth element are denoted by ρ_e and B_e, respectively, and the interpolation functions are $\phi_{e,1}$ and $\phi_{e,2}$; one reason for these reciprocal interpolations is that the inverses of the density and bulk modulus are used to formulate the finite element. Then we can consider the conditions from (24) to (26) that some potential interpolation functions should satisfy. In these conditions, the first and second design variables measure respectively how much rigid and porous material is in a finite element.

$$\text{Air: } (\gamma_{e,1},\gamma_{e,2}) = (0,0), (\phi_{e,1},\phi_{e,2}) = (0,0) \tag{24}$$

$$\text{Rigid: } (\gamma_{e,1},\gamma_{e,2}) = (1,0), (\phi_{e,1},\phi_{e,2}) = (1,0) \tag{25}$$

Table 1
The interpolation functions and their meanings.

$(\gamma_{e,1},\gamma_{e,2})$	Functions (27)	Functions (28)	Functions (29)	Functions (30)	Material
(0,0)	$(\phi_{e,1},\phi_{e,2})=(0,0)$	$(\phi_{e,1},\phi_{e,2})=(0,0)$	$(\phi_{e,1},\phi_{e,2})=(0,0)$	$(\phi_{e,1},\phi_{e,2})=(0,0)$	Air
(1,0)	$(\phi_{e,1},\phi_{e,2})=(1,0)$	$(\phi_{e,1},\phi_{e,2})=(1,0)$	$(\phi_{e,1},\phi_{e,2})=(1,0)$	$(\phi_{e,1},\phi_{e,2})=(1,0)$	Rigid
(0,1)	$(\phi_{e,1},\phi_{e,2})=(0,1)$	$(\phi_{e,1},\phi_{e,2})=(0,1)$	$(\phi_{e,1},\phi_{e,2})=(0,1)$	$(\phi_{e,1},\phi_{e,2})=(0,1)$	Porous
(1,1)	$(\phi_{e,1},\phi_{e,2})=(1,1)$ (Non-physical state)	$(\phi_{e,1},\phi_{e,2})=(1,0)$ (Rigid state)	$(\phi_{e,1},\phi_{e,2})=(0,1)$ (Porous state)	$(\phi_{e,1},\phi_{e,2})=(0,0)$ (Air state)	

$$\text{Porous: } (\gamma_{e,1},\gamma_{e,2})=(0,1),(\phi_{e,1},\phi_{e,2})=(0,1) \tag{26}$$

The basic and simple interpolation functions satisfying the above relationships are the linear functions:

$$\phi_{e,1}=\gamma_{e,1},\quad \phi_{e,2}=\gamma_{e,2} \tag{27}$$

With these interpolation functions, however, non-physical material representation can occur. In other words, with $(\gamma_{e,1},\gamma_{e,2})=(1,1)$, solid material and porous material appear at the same element, which is un-physical. To resolve this side effect and represent one state among air, rigid, or porous states distinctly, the following interpolation sets also satisfy the relationships from (24) to (26).

$$\text{Interpolation function set 1: } \phi_{e,1}=\gamma_{e,1},\quad \phi_{e,2}=\gamma_{e,2}(1-\gamma_{e,1}) \tag{28}$$

$$\text{Interpolation function set 2: } \phi_{e,1}=\gamma_{e,1}(1-\gamma_{e,2}),\quad \phi_{e,2}=\gamma_{e,2} \tag{29}$$

$$\text{Interpolation function set 3: } \phi_{e,1}=\gamma_{e,1}(1-\gamma_{e,2}),\quad \phi_{e,2}=\gamma_{e,2}(1-\gamma_{e,1}) \tag{30}$$

See Table 1 for the material states of the design variable combinations. As the optimizer uses the allowed solid or porous materials to minimize the objective function for better sound barriers, the state of $(\gamma_{e,1},\gamma_{e,2})=(1,1)$ would not occur with the interpolation functions (22)–(24).

In addition, we should consider whether the design variables converge to zero or one so that the associated finite elements are converged to one of three material states. Examining the convergence of the design variables in our numerical examples, we found that the three interpolation functions from (28) to (30) make all the design variables converge to zeros or ones. Any function set can be used. But among the three interpolation sets, we chose (28), which minimizes the object function best in the various optimization cases studied in the numerical section. With the interpolation function, the inverse density and inverse bulk modulus are expressed as follows:

$$\text{Inverse density: } \frac{1}{\rho_e(\gamma_{e,1},\gamma_{e,2})}=\frac{1}{\rho_a}+\left(\frac{1}{\rho_r}-\frac{1}{\rho_a}\right)\times\gamma_{e,1}+\left(\frac{1}{\rho_p}-\frac{1}{\rho_a}\right)\times\gamma_{e,2}(1-\gamma_{e,1}) \tag{31}$$

$$\text{Inverse bulk modulus: } \frac{1}{B_e(\gamma_{e,1},\gamma_{e,2})}=\frac{1}{B_a}+\left(\frac{1}{B_r}-\frac{1}{B_a}\right)\times\gamma_{e,1}+\left(\frac{1}{B_p}-\frac{1}{B_a}\right)\times\gamma_{e,2}(1-\gamma_{e,1}) \tag{32}$$

3.3. Sensitivity analysis

It is necessary to derive the sensitivity analysis to use the gradient-based optimization algorithm. With the complex pressure value, the SPL_r of (33) can be expressed as (34).

$$\mathrm{SPL}_r=10\log\frac{|p_r|^2}{|p_{reference}|^2} \tag{33}$$

$$\mathrm{SPL}_r=10\log\left[p_r\times\mathrm{conj}(p_r)\right]-10\log\left[p_{reference}\times\mathrm{conj}(p_{reference})\right],\ p_{reference}=2\times10^{-5}\ \mathrm{Pa} \tag{34}$$

where p_r is the complex sound pressure at the receiver point. By differentiating the SPL with respect to the design variables, the following formulations considering the conjugate of the pressure can be obtained [34].

$$\mathbf{S}=[\mathbf{K}-\omega^2\mathbf{M}+\mathrm{i}\omega\mathbf{F}^{radiation}]_{penalty},\quad \frac{\partial(\mathbf{Sp})}{\partial\gamma}=\mathbf{0} \tag{35}$$

$$\frac{\partial p_r}{\partial\gamma}=\mathbf{L}^{\mathrm{T}}\frac{\partial\mathbf{p}}{\partial\gamma} \tag{36}$$

where **L** is used to obtain the pressure value at the sound receiver point. Then the derivative of the SPL with respect to the design variable can be obtained using the Lagrangian multipliers.

$$\frac{\partial \mathrm{SPL}_r}{\partial \gamma} = 10\frac{\mathrm{conj}(p_r)\times \mathbf{L}^{\mathrm{T}}(\partial \mathbf{p}/\partial \gamma)}{p_r \times \mathrm{conj}(p_r)\times \ln 10}$$
$$+10\frac{p_r \times \mathbf{L}^{\mathrm{T}}(\partial \mathrm{conj}(p)/\partial \gamma)}{p_r \times \mathrm{conj}(p_r)\times \ln 10}+\boldsymbol{\lambda}_1^{\mathrm{T}}\left(\frac{\partial \mathbf{S}}{\partial \gamma}\mathbf{p}+\mathbf{S}\frac{\partial \mathbf{p}}{\partial \gamma}\right)+\boldsymbol{\lambda}_2^{\mathrm{T}}\left(\frac{\partial \mathrm{conj}(\mathbf{S})}{\partial \gamma}\mathrm{conj}(\mathbf{p})+\mathrm{conj}(\mathbf{S})\frac{\partial \mathrm{conj}(\mathbf{p})}{\partial \gamma}\right)$$
$$=\boldsymbol{\lambda}_1^{\mathrm{T}}\frac{\partial \mathbf{S}}{\partial \gamma}\mathbf{p}+\boldsymbol{\lambda}_2^{\mathrm{T}}\frac{\partial \mathrm{conj}(\mathbf{S})}{\partial \gamma}\partial\mathrm{conj}(\mathbf{p})=\boldsymbol{\lambda}_1^{\mathrm{T}}\frac{\partial \mathbf{S}}{\partial \gamma}\mathbf{p}+\mathrm{conj}(\boldsymbol{\lambda}_1)^{\mathrm{T}}\frac{\partial \mathrm{conj}(\mathbf{S})}{\partial \gamma}\mathrm{conj}(\mathbf{p})=2\times \mathrm{real}\left(\boldsymbol{\lambda}_1^{\mathrm{T}}\frac{\partial \mathbf{S}}{\partial \gamma}\mathbf{p}\right) \tag{37}$$

where the Lagrangian multipliers, $\boldsymbol{\lambda}_1$ and $\boldsymbol{\lambda}_2$, are defined as follows:

$$\mathbf{S}\boldsymbol{\lambda}_1=-10\frac{\mathrm{conj}(p_r)}{p_r\times \mathrm{conj}(p_r)\times \ln 10}\mathbf{L},\quad \mathrm{conj}(\mathbf{S})\boldsymbol{\lambda}_2=-10\frac{p_r}{p_r\times \mathrm{conj}(p_r)\times \ln 10}\mathbf{L},\quad \boldsymbol{\lambda}_2=\mathrm{conj}(\boldsymbol{\lambda}_1) \tag{38}$$

By summarizing the above equations, we can obtain the following sensitivity analysis.

$$\frac{\partial \mathrm{SPL}_r}{\partial \gamma}=-10\frac{\mathrm{conj}(p_r)}{p_r\times \mathrm{conj}(p_r)\times \ln 10}\mathbf{L}^{\mathrm{T}}\mathbf{S}^{-1}\frac{\partial \mathbf{S}}{\partial \gamma}\mathbf{p}+\mathrm{conj}\left[-10\frac{\mathrm{conj}(p_r)}{p_r\times \mathrm{conj}(p_r)\times \ln 10}\mathbf{L}^{\mathrm{T}}\mathbf{S}^{-1}\frac{\partial \mathbf{S}}{\partial \gamma}\mathbf{p}\right] \tag{39}$$

4. Noise barrier design examples

To investigate the validity and applicability of the developed optimization procedure, we considered the basic analysis and design domain shown in Fig. 8. It consists of a noise source close to the ground and a typical straight barrier with a design domain at its top, designed to reduce the noise level for nearby pedestrians and cyclists. At a distance of X_{SB} from a center sound source, the square design domain (1.025 m by 1 m) is located at the end of the straight barrier and discretized by 0.025 m × 0.025 m finite elements. At a distance of X_{SR} from the sound source, a sound receiver is located, and the source pressure at the receiver is set for the objective function. By finding the optimal distributions of porous and rigid materials, their different acoustic properties can be used to minimize the SPL at the receiver point. To obtain consistent acoustic behavior in the objective function, the frequency of the sound source is set to 100 Hz.

4.1. Example 1: The effect of the interpolation functions

First of all, we investigated the effects of the interpolation function sets (28)–(30) on optimal layouts. For the initial geometrical conditions, we located the 1 m tall straight barrier. The allowable mass ratios of rigid and porous materials to the design domain are both 3percent. With the present optimization method, some results are given in Fig. 9. The black and the gray are used to render rigid and porous domains, respectively. With the first interpolation function set, the typical T-bar structure appears with the porous material structures at the ends of the rigid bar. With the second and third interpolation function sets, the porous material emerges at the end of the bar and a starfish-shaped rigid structure emerges. From an objective point of view, the optimization using the first interpolation function set shows the best result. In addition, with the first function set, the typical T-bar type structure appears. Existing acoustic research has concluded that the T-shape structure is one of optimal layouts, and the present optimization process found it easily.

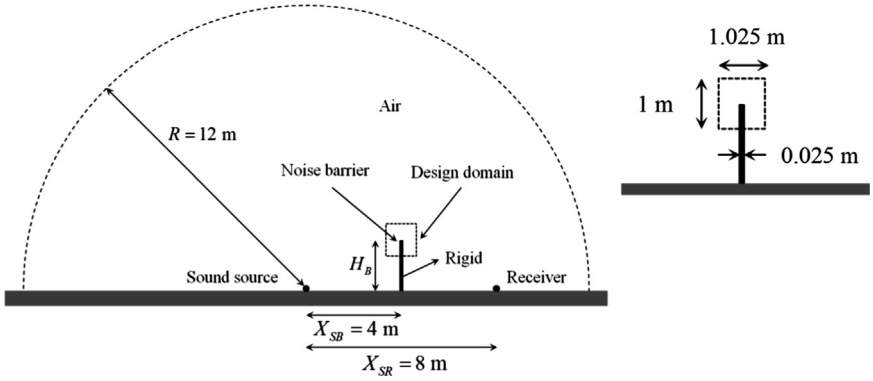

Fig. 8. Position and size of the design domain around a straight rigid barrier ($\rho_a = 1.25\ \mathrm{kg}/m^3$, $c_a = 343\ m/s$ and $f = 100$ Hz).

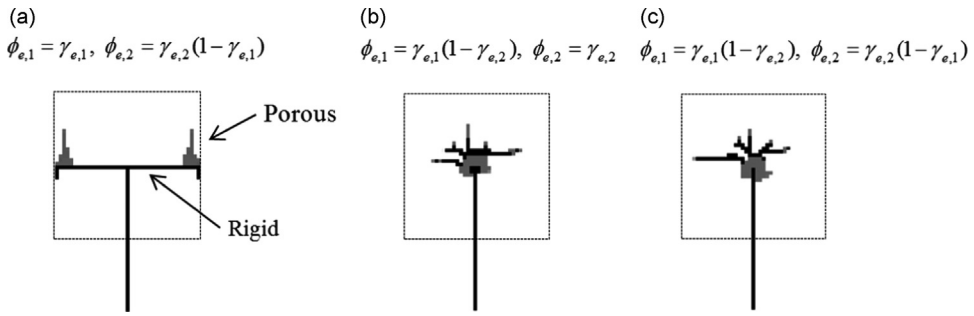

Fig. 9. Optimization results with the interpolation functions for a 1 m basic barrier (3percent rigid (black), 3percent porous (gray)). (a) Interpolation function set 1 ($\phi_{e,1}=\gamma_{e,1}, \phi_{e,2}=\gamma_{e,2}(1-\gamma_{e,1})$, $SPL_r=63.74$ dB), (b) interpolation function set 2 ($\phi_{e,1}=\gamma_{e,1}(1-\gamma_{e,2}), \phi_{e,2}=\gamma_{e,2}$, $SPL_r=67.10$ dB), and (c) interpolation function set 3 ($\phi_{e,1}=\gamma_{e,1}(1-\gamma_{e,2}), \phi_{e,2}=\gamma_{e,2}(1-\gamma_{e,1})$, $SPL_r=67.16$ dB).

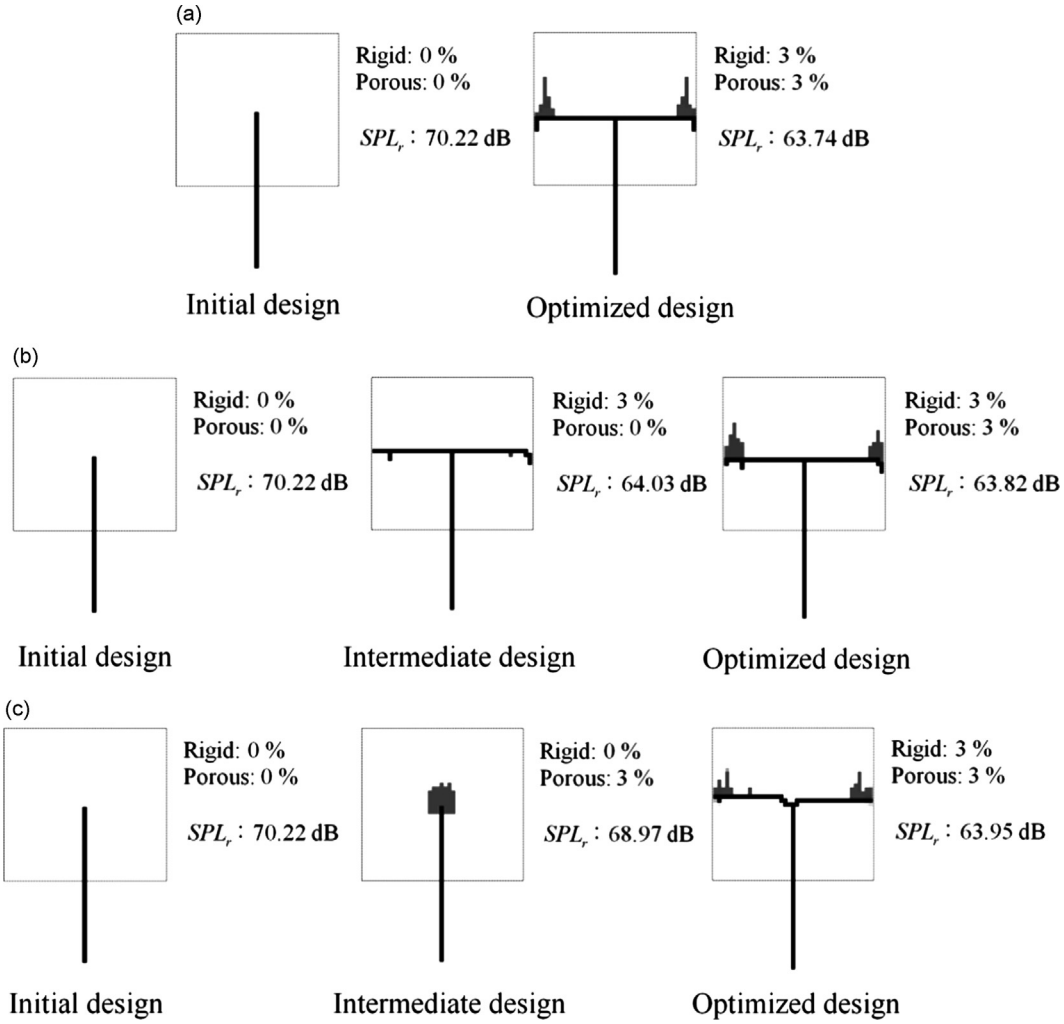

Fig. 10. Optimization results with the initial design for a 1 m basic barrier. (Black: rigid material, gray: porous material). (a) Distributing two materials simultaneously, (b) distributing rigid material first and porous material later, and (c) distributing porous material first and rigid material later.

4.2. Example 2: Local optima issue and optimization strategy

From an objective point of view, the first interpolation function set shows the best performance by more than 3 dB (Fig. 9). Thus we will present the further investigations with the first interpolation function set for different optimization conditions and strategies.

As many local optima exist in TO, it is possible to introduce some optimization strategies with different initial designs. In the previous optimization example, rigid and porous materials were optimized and distributed simultaneously with uniform distributions of the design variables. To exploit the locality of the objective function, one of the two materials could be distributed first, and the optimal distribution of the other variables can follow. If different designs are obtained in this way, it would reveal the existence of local optima within the mathematical problem. If one optimization strategy gives better designs, we can choose it. Fig. 10(a: right) shows the optimization result obtained by distributing the two materials simultaneously from the initial straight bar design in Fig. 10(a: left). Next, Fig. 10(b: center) shows the optimization result obtained by distributing only rigid material from Fig. 10(b: left). In this first optimization process, only the design variables representing the rigid material ratio in each element are optimized. With the 3percent usage of rigid material, a typical T-bar structure is obtained. By setting this design as an initial design, the distribution of porous material is tested in Fig. 10(b: right). In this optimization procedure, all design variables representing the mass ratios of rigid and porous materials in each element are optimized again for Fig. 10(b: right). On the other hand, Fig. 10(c: center) shows the optimization result obtained by distributing only porous material from Fig. 10(c: left). With the 3percent usage, porous material appears at the end of the straight bar. We again set this design with only porous material as an initial design and tested the distribution of the rigid material in Fig. 10(c: right). In this design process, all design variables are optimized again to find out the best layout. In the three cases, material layouts appear similar to one another and also have similar objective values. Note that the rigid material distributions in Fig. 10(a–c: right) are also similar to a T-shaped barrier. Porous material is located on both sides of the upper surface of the rigid T-shaped barrier. We can postulate that the priority of either rigid or porous material has little effect on the optimum layout in this particular example with these particular boundary conditions.

Fig. 11 shows the SPL distributions before and after the optimizations. Fig. 11(a) shows the pressure before the optimization in Fig. 10(a–c: left); Fig. 11(b) shows the pressure after the optimization in Fig. 10(a: right). The sound pressure

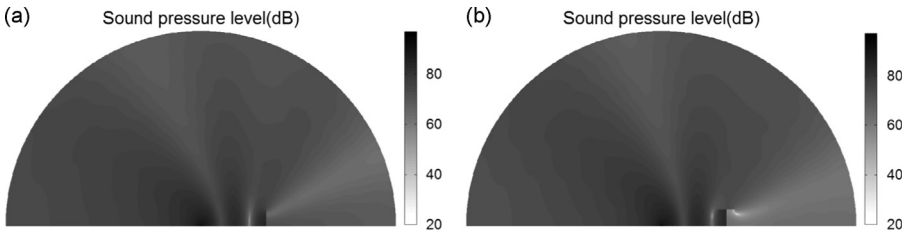

Fig. 11. (a) SPL distribution of the initial design in Fig. 10(a: left) and (b) SPL distribution of the design result with both rigid and porous materials in Fig. 10 (a: right).

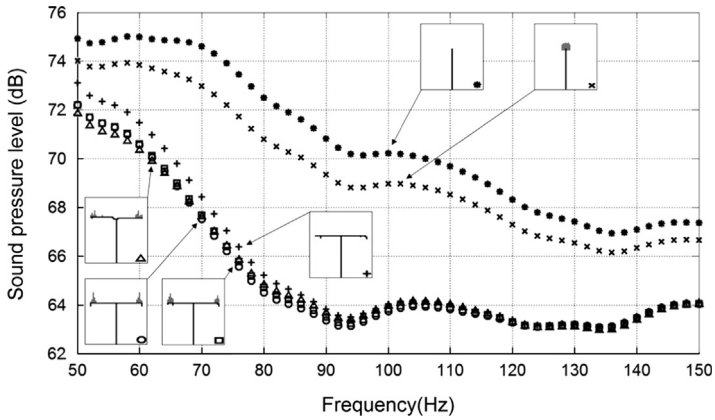

Fig. 12. Frequency responses of the design results shown in Fig. 10.

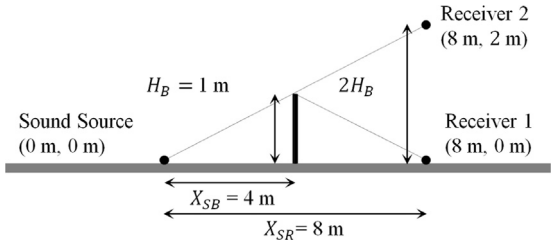

Fig. 13. Positions of the two sound receivers.

magnitude behind the barrier is much lower after the optimization. Fig. 12 shows the frequency responses of the designs in Fig. 10. From this comparison, it is observed that the effect of the rigid body on the objective function is much more significant than that of the porous material.

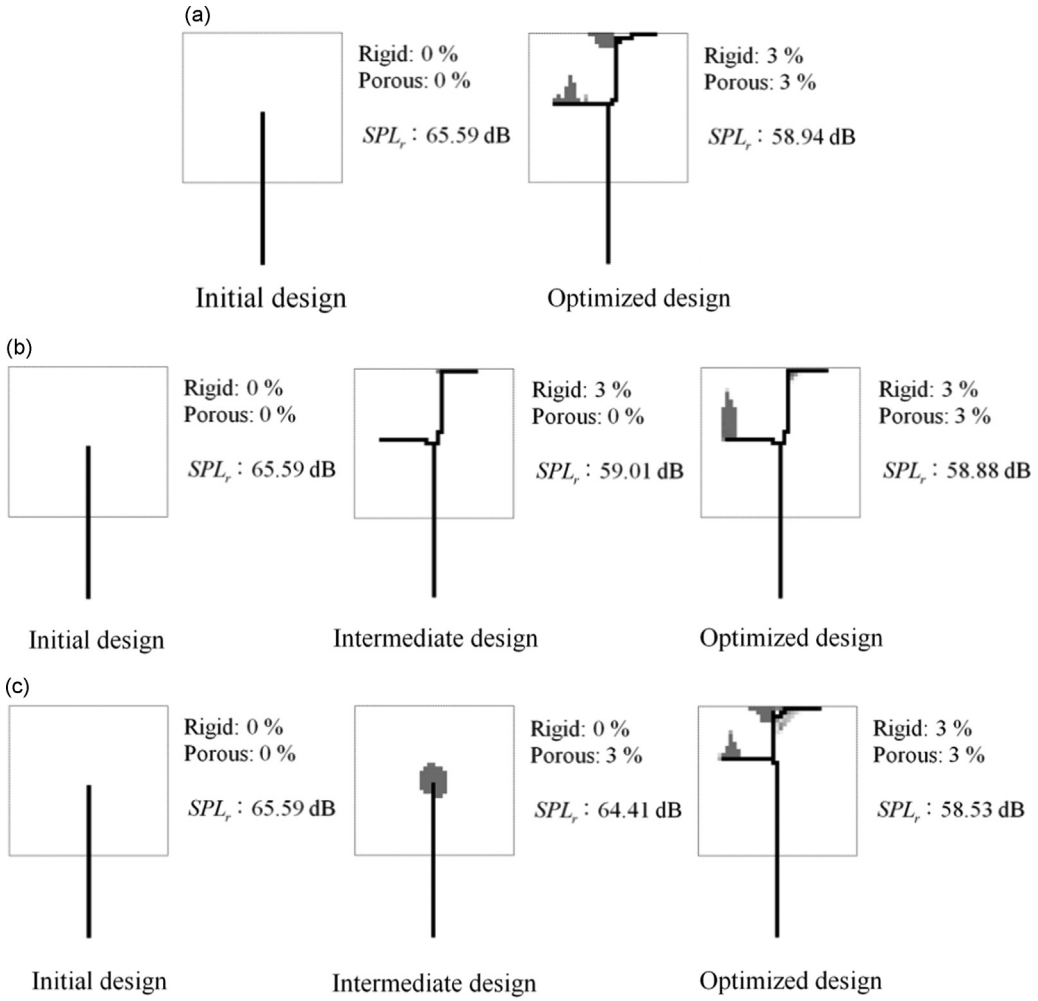

Fig. 14. Optimization results with different receiver positions. (black: rigid material, gray: porous material). (a) Distributing two materials simultaneously, (b) distributing rigid material first and porous material later, and (c) distributing porous material first and rigid material later.

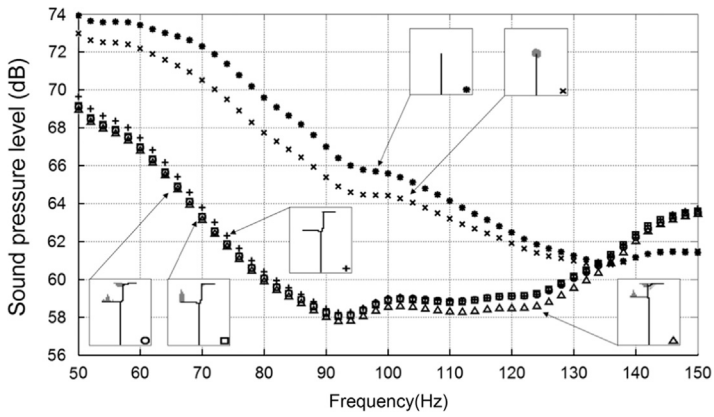

Fig. 15. Frequency response functions of the design results in Fig. 14.

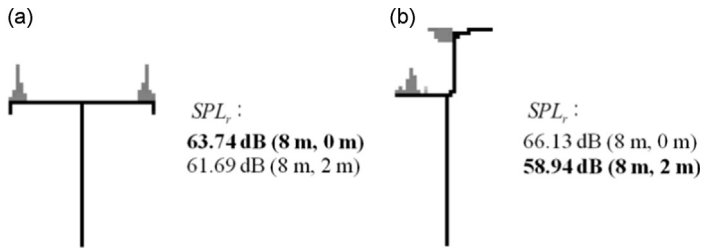

Fig. 16. Optimization results with two different receiver positions. (a) Receiver 1 (8 m, 0 m) and (b) receiver 2 (8 m, 2 m).

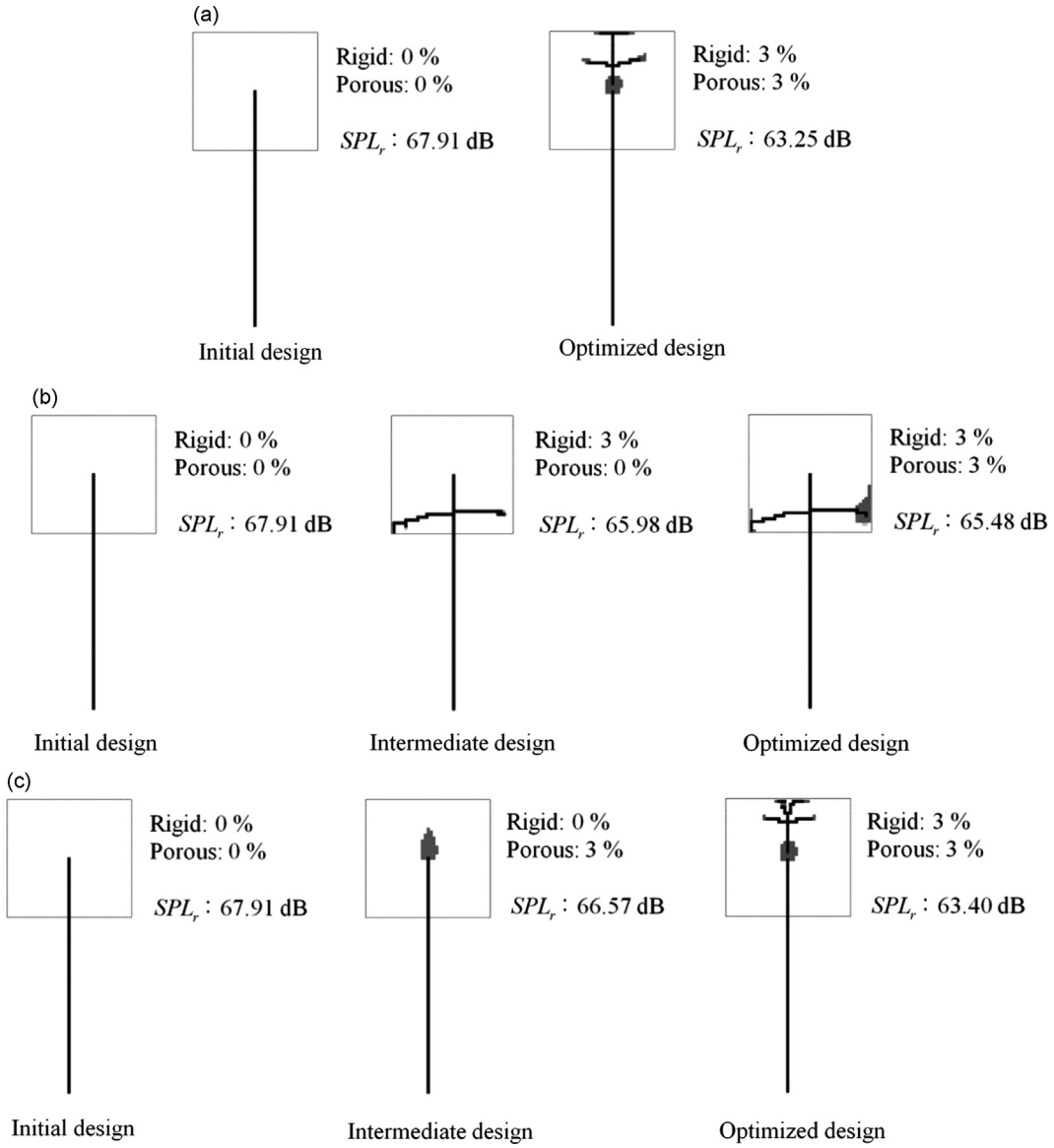

Fig. 17. Optimization results with the initial design for a 2 m basic barrier ((8 m, 0 m): receiver position to minimize SPL). (a) Distributing two materials simultaneously, (b) distributing rigid material first and porous material later, and (c) distributing porous material first and rigid material later.

4.3. Example 3: Optimization results with different sound receiver positions

Common acoustic engineering designs rely on heuristic trial and error. Because this takes a long time, advanced design methods that take into account uncertainties, such as the material property uncertainty and the boundary condition uncertainty, should be developed. As the present forward and the sensitivity analyses adopt the acoustic finite element

procedure and the adjoint variable method, new designs considering various physical conditions can be obtained with moderate computation time. To show this, a new design problem with a different position of the sound receiver is presented in Fig. 13. The new sound receiver (Receiver 2) is located 2 m above the rigid ground. Note that the sound travel distance from the sound source to receivers 1 and 2 is the same.

Fig. 14 shows some optimized sound barriers for the new receiver 2. It is interesting that the T-shape is no longer optimal. The inclined y-shaped barrier becomes an optimal layout. The investigation of the SPL reveals that the rigid structure designed by the present optimization method blocks the acoustic wave propagation toward receiver 2 more effectively than the T-shape structure. The optimal layout with only porous material for receiver 2, Fig. 14(c: center), is similar to that for receiver 1. Optimizing both rigid and porous materials simultaneously, the design of Fig. 14(a: right) is obtained, and it is not surprising that the rigid structure of Fig. 14(a: right) is similar to that of the design with only a rigid body (Fig. 14(b: center)). Physically it seems that because the effect of the rigid material is much larger than that of the porous material, the optimizer places the rigid material first and then places the porous material. Similar to the porous material distributions of the first example, the porous material is distributed at the end sides of the rigid bar structures in Fig. 14(b: right). Comparing the layouts optimized by the different optimizing strategies and their objective values, it seems that the optimization strategies, i.e., rigid and porous design simultaneously, rigid design after porous design, and vice versa, provide similar designs for this example. It indirectly indicates that the design space has become almost convex, and the similar designs are obtained with different initial designs. It also indicates the applicability of the present optimization procedure in finding optimal layouts with different boundary conditions. Fig. 15 shows the frequency response functions of the optimized results of Fig. 14. For the excitation frequencies above 130 Hz, the original straight bar is much more efficient than the optimized barriers (Fig. 14). But at the excitation frequency, 100 Hz, the SPL of 66 dB in the initial design is reduced by more than 60 dB, which illustrates one important aspect of sound barriers: they can increase the SPL in some specific excitation frequency ranges while decreasing the overall SPL.

Fig. 16 compares the optimization results of the two different receiver positions of Fig. 10 (receiver position: (8 m, 0 m)) and Fig. 14 (receiver position: (8 m, 2 m)). By comparing the SPLs of the two designs at each receiver position, it is notable that each design shows lower SPLs at its receiver position.

4.4. Example 4: Optimization results with different initial barrier heights (2 m and 3 m initial poles)

As a next numerical example, the effect of the height of the initial rigid barrier is studied. Without loss of generality, Figs. 17 and 19 show the optimization results with 2 m and 3 m straight barriers, respectively, for the (8 m, 0 m) receiver position. Again, the three optimization strategies are applied, and the different optimized layouts are obtained (Figs. 18 and 20). The results indicate that with taller rigid barriers, the local optima issue becomes serious. Specifically, the optimization result with only rigid material in Fig. 17(b) shares some similarities with a T-shaped barrier profile. But the optimization result with a 3 m initial barrier in Fig. 19(b) becomes an exact T-shaped barrier again. Porous material appears at the ends of the horizontal arms of the designs.

4.5. Example 5: Optimization results with different flow resistivity values

The last numerical example tests the effect of the flow resistivity value, σ, in the Delany–Bazley model formulated in (15) and (16). Fig. 21 shows the optimization layouts with different flow resistivity values. The geometrical conditions and material properties, except for the flow resistivity values, are the same as those in Figs. 10 and 14. The different airflow resistivity values clearly influence the pressure attenuation and optimization process.

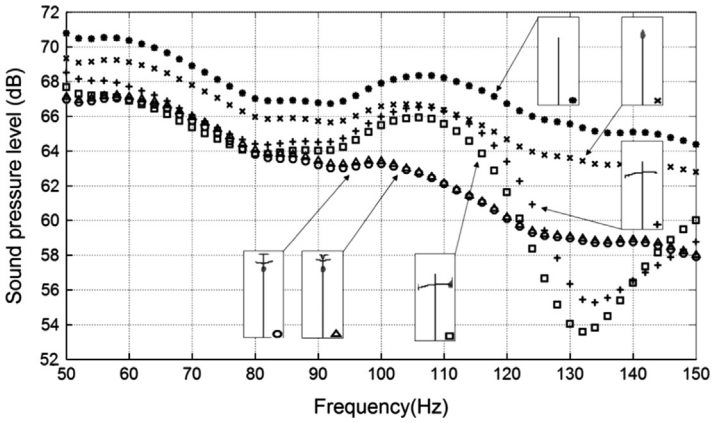

Fig. 18. Frequency response functions of the design results in Fig. 17.

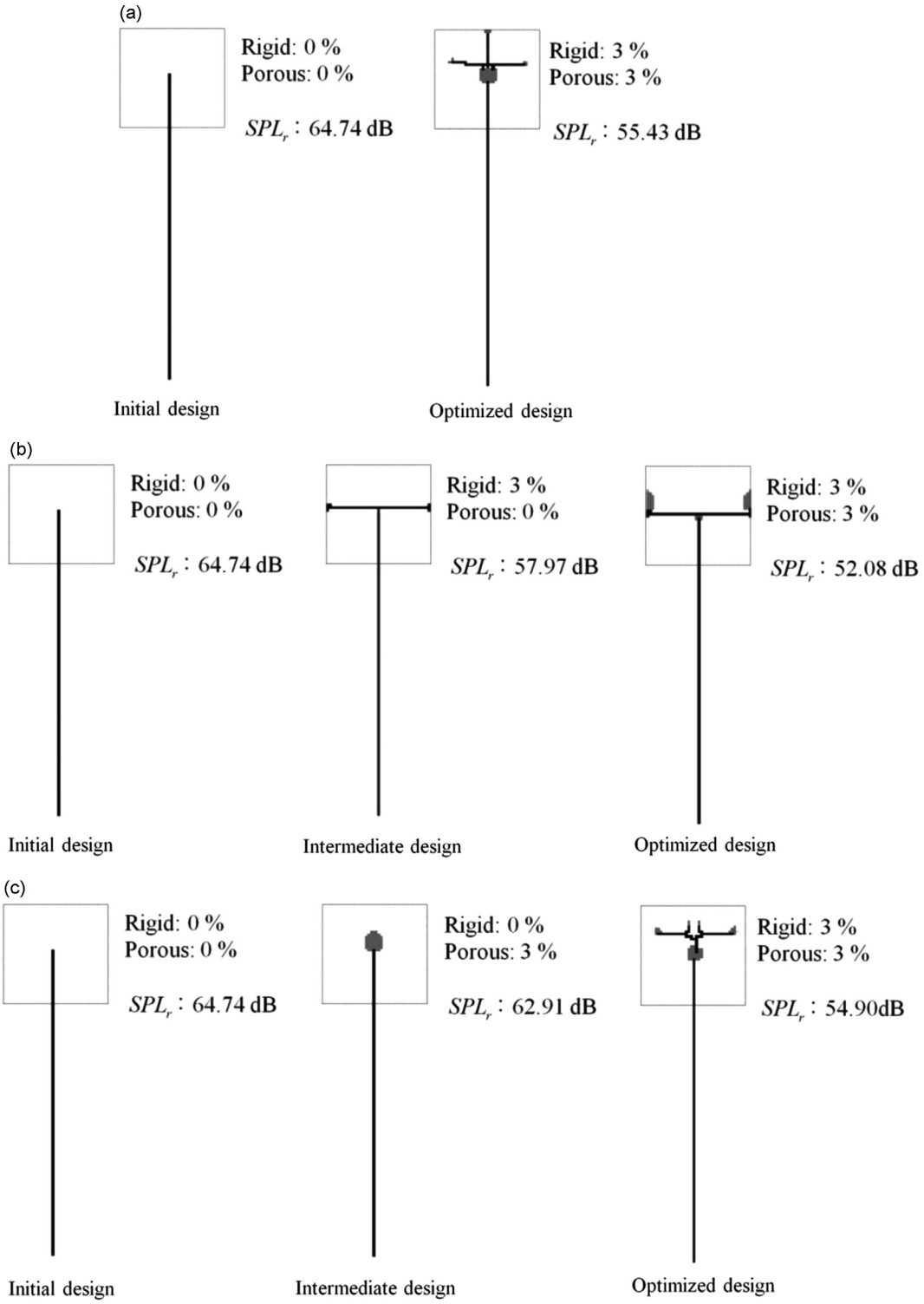

Fig. 19. Optimization results with the initial design for a 3 m basic barrier ((8 m, 0 m): receiver position to minimize SPL). (a) Distributing two materials simultaneously, (b) distributing rigid material first and porous material later, and (c) distributing porous material first and rigid material later.

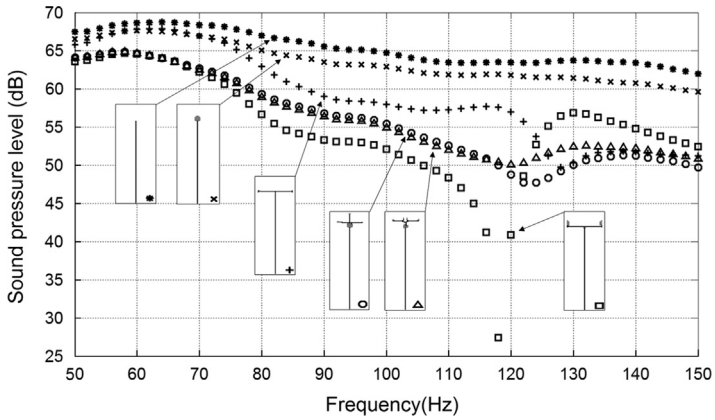

Fig. 20. Frequency response functions of the design results in Fig. 19.

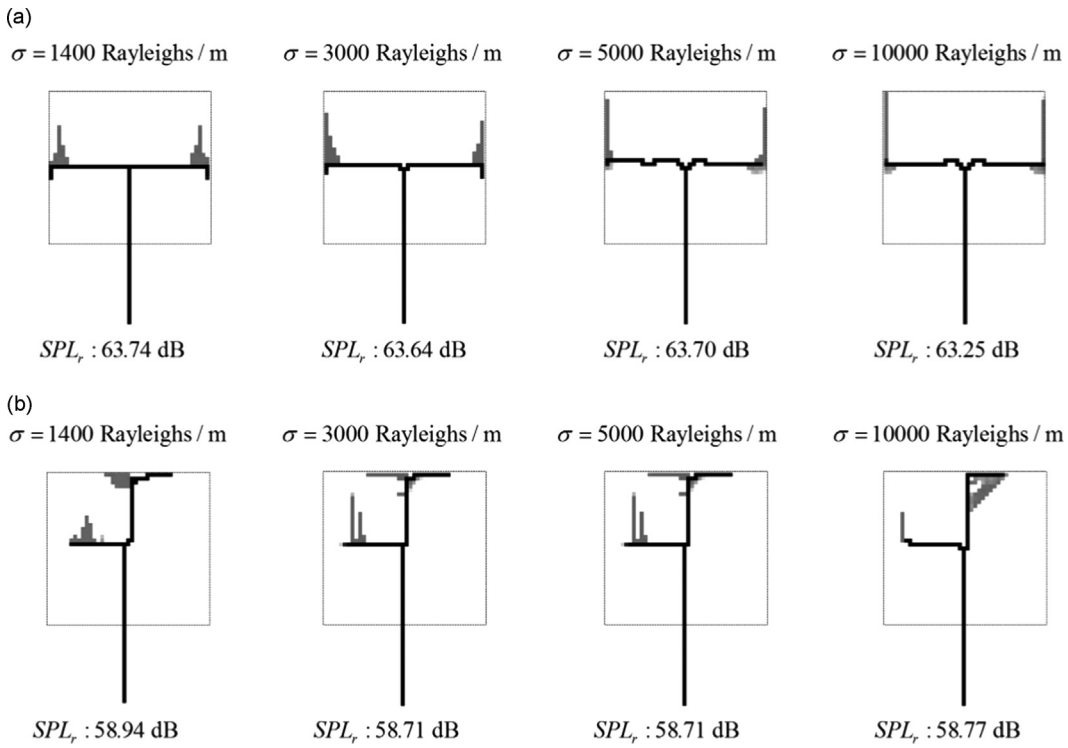

Fig. 21. Optimization results with different flow-resistivity values for the porous material for a 1 m basic barrier. Receiver position to minimize SPL is (8 m, 0 m) from source position for (a) and (8 m, 2 m) for (b).

4.6. Example 6: optimization results for higher frequencies

To show the applicability of the present approach for higher frequencies, the following numerical examples are considered. In Figs. 22 and 23, the optimization problems are solved for 200 Hz and 300 Hz, respectively. As shown, some interesting designs can be obtained by the present approach.

5. Conclusion

This research applies the ATO method to the optimal design of noise barriers considering both rigid and porous materials. Commonly, the typical T-shaped noise barrier is used for better barrier performance. Some relevant research has studied the

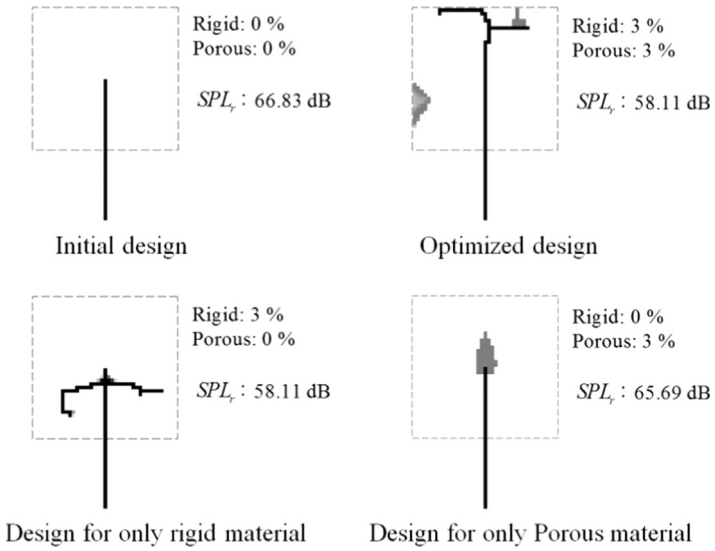

Fig. 22. Optimization results with the initial design for 1 m basic barrier for sound source of 200 Hz (receiver position is (8 m, 0 m) from the source position).

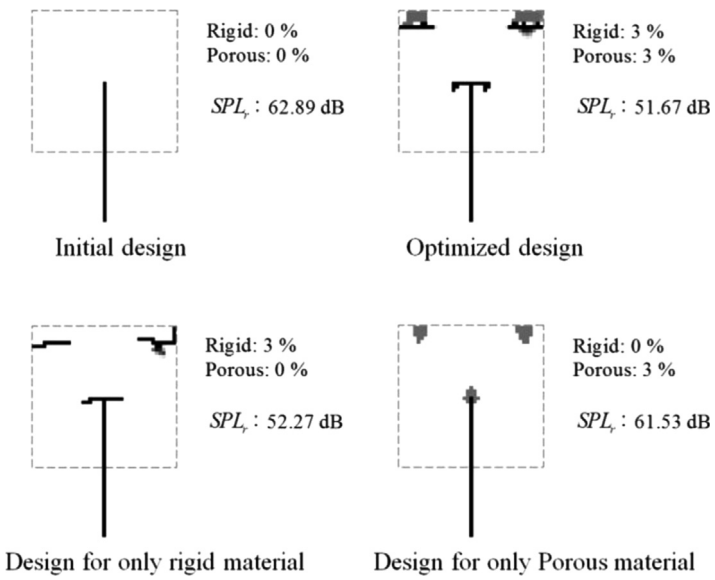

Fig. 23. Optimization results with the initial design for 1 m basic barrier for sound source of 300 Hz (receiver position is (8 m, 0 m) from the source position).

inclusion of diffusers or porous materials at the top of the T-shaped barrier. In addition, size and shape optimization requiring initial designs have been conducted to improve the performance of noise barriers. To overcome the limitations of requiring initial designs and to allow topological changes, we have developed and applied the ATO method.

The topology optimization process in this research consists of finite element analysis, adjoint-sensitivity analysis, and the optimization process. To consider pressure attenuation from the porous material, the Delany–Bazley material model was implemented. To design the optimal position of the porous material as well as that of rigid material, three interpolation function sets were tested. Furthermore, by applying the present ATO method, we successfully designed some optimal sound barriers. In the first example, the effects of the interpolation functions on the optimum layout were investigated. Among the suggested interpolation function sets, one was selected by comparing the objective function values of each interpolation function. In the next example, the optimization strategies with different initial and intermediate designs were developed. We found that it is better to design the rigid material before the porous material in topology optimization. We also tested

the effect of receiver position. When we moved the sound receiver, the T-shaped sound barrier was no longer the most effective shape. We also tested the effects of the heights of the lower straight bars.

In conclusion, we developed an optimization process for sound barrier design with rigid and porous materials. By finding optimal solutions, the validity and the applicability of the present optimization method have been demonstrated.

Acknowledgments

This work was supported by the Global Frontier R&D Program on Center for Wave Energy Control based on Metamaterials funded by the National Research Foundation under the Ministry of Science, ICT & Future Planning, Korea (No. 2014063711).

References

[1] C. Cianfrini, M. Corcione, L. Fontana, Experimental verification of the acoustic performance of diffusive roadside noise barriers, *Applied Acoustics* 68 (2007) 1357–1372.
[2] G.R. Watts, Acoustic performance of parallel traffic noise barriers, *Applied Acoustics* 47 (1996) 95–119.
[3] G.R. Watts, D.H. Crombie, D.C. Hothersall, Acoustic performance of new designs of traffic noise barriers – full-scale tests, *Journal of Sound and Vibration* 177 (1994) 289–305.
[4] T. Ishizuka, K. Fujiwara, Performance of noise barriers with various edge shapes and acoustical conditions, *Applied Acoustics* 65 (2004) 125–141.
[5] K. Fujiwara, D.C. Hothersall, C. Kim, Noise barriers with reactive surfaces, *Applied Acoustics* 53 (1998) 255–272.
[6] T. Okubo, K. Yamamoto, Procedures for determining the acoustic efficiency of edge-modified noise barriers, *Applied Acoustics* 68 (2007) 797–819.
[7] W. Shao, H.P. Lee, S.P. Lim, Performance of noise barriers with random edge profiles, *Applied Acoustics* 62 (2001) 1157–1170.
[8] D.C. Hothersall, S.N. Chandlerwilde, M.N. Hajmirzae, Efficiency of single noise barriers, *Journal of Sound and Vibration* 146 (1991) 303–322.
[9] G.R. Watts, Acoustic performance of a multiple edge noise barrier profile at motorway sites, *Applied Acoustics* 47 (1996) 47–66.
[10] G.R. Watts, P.A. Morgan, Acoustic performance of an interference-type noise-barrier profile, *Applied Acoustics* 49 (1996) 1–16.
[11] M.R. Monazzam, Y.W. Lam, Performance of profiled single noise barriers covered with quadratic residue diffusers, *Applied Acoustics* 66 (2005) 709–730.
[12] M. Naderzadeh, M.R. Monazzam, P. Nassiri, S.M.B. Fard, Application of perforated sheets to improve the efficiency of reactive profiled noise barriers, *Applied Acoustics* 72 (2011) 393–398.
[13] D.J. Oldham, C.A. Egan, A parametric investigation of the performance of T-profiled highway noise barriers and the identification of a potential predictive approach, *Applied Acoustics* 72 (2011) 803–813.
[14] D. Duhamel, Shape optimization of noise barriers using genetic algorithms, *Journal of Sound and Vibration* 297 (2006) 432–443.
[15] D. Greiner, J.J. Aznarez, O. Maeso, G. Winter, Single- and multi-objective shape design of Y-noise barriers using evolutionary computation and boundary elements, *Advances in Engineering Software* 41 (2010) 368–378.
[16] S. Mun, Y.H. Cho, Noise barrier optimization using a simulated annealing algorithm, *Applied Acoustics* 70 (2009) 1094–1098.
[17] M. Baulac, J. Defrance, P. Jean, Optimisation with genetic algorithm of the acoustic performance of T-shaped noise barriers with a reactive top surface, *Applied Acoustics* 69 (2008) 332–342.
[18] S. Grubesa, K. Jambrosic, H. Domitrovic, Noise barriers with varying cross-section optimized by genetic algorithms, *Applied Acoustics* 73 (2012) 1129–1137.
[19] M.P. Bendsoe, N. Kikuchi, Generating optimal topologies in structural design using a homogenization method, *Computer Methods in Applied Mechanics and Engineering* 71 (1988) 197–224.
[20] M.P. Bendsøe, O. Sigmund, *Topology Optimization: Theory, Methods, and Applications*, Springer, Berlin; New York, 2003.
[21] J.S. Lee, E. Kim, Y.Y. Kim, J.S. Kim, Y.J. Kang, Optimal poroelastic layer sequencing for sound transmission loss maximization by topology optimization method, *Journal of the Acoustical Society of America* 122 (2007) 2097–2106.
[22] J. Lee, S.Y. Wang, A. Dikec, Topology optimization for the radiation and scattering of sound from thin-body using genetic algorithms, *Journal of Sound and Vibration* 276 (2004) 899–918.
[23] G.H. Yoon, J.S. Jensen, O. Sigmund, Topology optimization of acoustic–structure interaction problems using a mixed finite element formulation, *International Journal for Numerical Methods in Engineering* 70 (2007) 1049–1075.
[24] J.S. Lee, Y.Y. Kim, J.S. Kim, Y.J. Kang, Two-dimensional poroelastic acoustical foam shape design for absorption coefficient maximization by topology optimization method, *Journal of the Acoustical Society of America* 123 (2008) 2094–2106.
[25] T. Yamamoto, S. Maruyama, S. Nishiwaki, M. Yoshimura, Topology design of multi-material soundproof structures including poroelastic media to minimize sound pressure levels, *Computer Methods in Applied Mechanics and Engineering* 198 (2009) 1439–1455.
[26] J.B. Du, N. Olhoff, Minimization of sound radiation from vibrating bi-material structures using topology optimization, *Structural and Multidisciplinary Optimization* 33 (2007) 305–321.
[27] E. Wadbro, M. Berggren, Topology optimization of an acoustic horn, *Computer Methods in Applied Mechanics and Engineering* 196 (2006) 420–436.
[28] R.Z. Yang, J.B. Du, Microstructural topology optimization with respect to sound power radiation, *Structural and Multidisciplinary Optimization* 47 (2013) 191–206.
[29] L. Shu, M.Y. Wang, Z.D. Ma, Level set based topology optimization of vibrating structures for coupled acoustic-structural dynamics, *Computers & Structures* 132 (2014) 34–42.
[30] L.R. Lu, T. Yamamoto, M. Otornori, T. Yamada, K. Izui, S. Nishiwaki, Topology optimization of an acoustic metamaterial with negative bulk modulus using local resonance, *Finite Elements in Analysis and Design* 72 (2013) 1–12.
[31] W. Akl, A. El-Sabbagh, K. Al-Mitani, A. Baz, Topology optimization of a plate coupled with acoustic cavity, *International Journal of Solids and Structures* 46 (2009) 2060–2074.
[32] M.B. Duhring, J.S. Jensen, O. Sigmund, Acoustic design by topology optimization, *Journal of Sound and Vibration* 317 (2008) 557–575.
[33] J. Kook, K. Koo, J. Hyun, J.S. Jensen, S. Wang, Acoustical topology optimization for Zwicker's loudness model – application to noise barriers, *Computer Methods in Applied Mechanics and Engineering* 237 (2012) 130–151.
[34] G.H. Yoon, Acoustic topology optimization of fibrous material with Delany–Bazley empirical material formulation, *Journal of Sound and Vibration* 332 (2013) 1172–1187.
[35] H. Saunders, Fundamentals of Acoustics, 3rd ed. – L.E. Kinsler, A.R. Frey, H.B. Coppens,, J.V. Sanders, *Journal of Vibration and Acoustics* 105 (1983) 269–270.
[36] J.W. Lee, Y.Y. Kim, Topology optimization of muffler internal partitions for improving acoustical attenuation performance, *International Journal for Numerical Methods in Engineering* 80 (2009) 455–477.
[37] M.E. Delany, E.N. Bazley, Acoustical properties of fibrous absorbent materials, *Applied Acoustics* 3 (1970) 105–116.
[38] J.F. Allard, N. Atalla, *Propagation of Sound in Porous Media: Modelling Sound Absorbing Materials*, 2nd ed. Wiley, Hoboken, N.J., 2009.
[39] K.O. Ballagh, Acoustical properties of wool, *Applied Acoustics* 48 (1996) 101–120.

[40] H.Y.T. Phan, T. Yano, T. Sato, T. Nishimura, Characteristics of road traffic noise in Hanoi and Ho Chi Minh City, Vietnam, *Applied Acoustics* 71 (2010) 479–485.
[41] A. Can, L. Leclercq, J. Lelong, D. Botteldooren, Traffic noise spectrum analysis: dynamic modeling vs. experimental observations, *Applied Acoustics* 71 (2010) 764–770.
[42] A.J. Torija, D.P. Ruiz, Using recorded sound spectra profile as input data for real-time short-term urban road-traffic-flow estimation, *Science of the Total Environment* 435 (2012) 270–279.
[43] K. Svanberg, The method of moving asymptotes – a new method for structural optimization, *International Journal for Numerical Methods in Engineering* 24 (1987) 359–373.
[44] J.W. Lee, Y.Y. Kim, Rigid body modeling issue in acoustical topology optimization, *Computer Methods in Applied Mechanics and Engineering* 198 (2009) 1017–1030.